

# From star-forming spirals to passive spheroids: integral field spectroscopy of E+A galaxies

A. M. Swinbank,<sup>1\*</sup> M. L. Balogh,<sup>2</sup> R. G. Bower,<sup>1</sup> A. I. Zabludoff,<sup>3</sup> J. R. Lucey,<sup>1</sup>  
S. L. McGee,<sup>1</sup> C. J. Miller<sup>4</sup> and R. C. Nichol<sup>5</sup>

<sup>1</sup>*Institute for Computational Cosmology, Department of Physics and Astronomy, University of Durham, South Road, Durham DH1 3LE*

<sup>2</sup>*Department of Physics, University of Waterloo, Waterloo, ON N2L 3G1, Canada*

<sup>3</sup>*Steward Observatory, University of Arizona, 933 North Cherry Avenue, Tucson, AZ 85721-0065, USA*

<sup>4</sup>*Astronomy Department, University of Michigan, Ann Arbor, MI 48109, USA*

<sup>5</sup>*Institute for Cosmology and Gravitation, Mercantile House, Hampshire Terrace, University of Portsmouth, Portsmouth PO1 2EG*

Accepted 2011 October 25. Received 2011 October 25; in original form 2011 July 29

## ABSTRACT

We present three-dimensional spectroscopy of 11 E+A galaxies at  $z = 0.06$ – $0.12$ . These galaxies were selected for their strong H $\delta$  absorption but weak (or non-existent) [O II]  $\lambda 3727$  and H $\alpha$  emission. This selection suggests that a recent burst of star formation was triggered but subsequently abruptly ended. We probe the spatial and spectral properties of both the young ( $\lesssim 1$  Gyr) and old ( $\gtrsim$  few Gyr) stellar populations. Using the H $\delta$  equivalent widths we estimate that the burst masses must have been at least 10 per cent by mass ( $M_{\text{burst}} \gtrsim 10^{10} M_{\odot}$ ), which is also consistent with the star formation history inferred from the broad-band spectral energy distributions. On average the A stars cover  $\sim 33$  per cent of the galaxy image, extending over  $2$ – $15$  kpc<sup>2</sup>, indicating that the characteristic E+A signature is a property of the galaxy as a whole and not due to a heterogeneous mixture of populations. In approximately half of the sample, we find that the A stars, nebular emission and continuum emission are not co-located, suggesting that the newest stars are forming in a different place than those that formed  $\lesssim 1$  Gyr ago, and that recent star formation has occurred in regions distinct from the oldest stellar populations. At least 10 of the galaxies (91 per cent) have dynamics that class them as ‘fast rotators’ with magnitudes,  $v/\sigma$ ,  $\lambda_R$  and bulge-to-total (B/T) ratio comparable to local, representative ellipticals and S0s. We also find a correlation between the spatial extent of the A stars and the dynamical state of the galaxy such that the fastest rotators tend to have the most compact A star populations, providing new constraints on models that aim to explain the transformation of later type galaxies into early types. Finally, we show that there are no obvious differences between the line extents and kinematics of E+A galaxies detected in the radio (active galactic nucleus, AGN) compared to non-radio sources, suggesting that AGN feedback does not play a dramatic role in defining their properties, and/or that its effects are short.

**Key words:** galaxies: evolution – galaxies: kinematics and dynamics – galaxies: starburst – galaxies: stellar content.

## 1 INTRODUCTION

Galaxies with strong Balmer absorption lines in their spectra, but weak nebular emission (such as [O II]  $\lambda 3727$  Å), represent a short-lived but potentially important phase in galaxy evolution (e.g. Tran et al. 2003, 2004). These ‘E+A’ galaxies have strong absorption lines (such as H $\delta$ ), representing a stellar population dominated by A stars, which are either absent or overwhelmed by the much brighter OB stars in most galaxies. These signatures suggest that the star formation within the galaxy abruptly ended  $\lesssim 1$  Gyr ago, possibly

following a starburst phase. It is likely that a variety of physical mechanisms lead to such a stellar population (e.g. Dressler & Gunn 1982; Couch & Sharples 1987; Zabludoff et al. 1996; Balogh et al. 1999; Poggianti et al. 1999), but most invoke a major transformation from one galaxy type to another, possibly representing an evolutionary link between gas-rich, star-forming galaxies and quiescent spheroids. Although such galaxies are very rare in the local Universe, their short lifetime means they could potentially represent an important phase in the evolution of most normal galaxies (e.g. Zabludoff et al. 1996; Yan et al. 2009).

In order to trace the route by which star-forming galaxies evolve into quiescent systems, there are several issues which must be addressed. First, from where in the galaxy does the unusual spectrum

\*E-mail: a.m.swinbank@dur.ac.uk

originate? Is the strong H $\delta$  a result of galaxy-wide A-star populations, or is it due to a heterogeneous mixture of populations, such as a nuclear starburst with a very high equivalent width ( $>10 \text{ \AA}$ ) on top of an otherwise normal galaxy? Secondly, what star formation history leads to the spectral characteristics of these galaxies? Is the E+A phase related to a significant enhancement of the star formation, or simply the rapid decline of star formation in normal, gas-rich galaxies. Finally, what triggers the recent change in star formation history?

Several physical mechanisms have been suggested for the triggering (and subsequent rapid end) of starbursts in field E+A galaxies, including major mergers (Mihos & Hernquist 1996) and unequal mass mergers and tidal interactions (Bekki et al. 2005; Pracy et al. 2005). Recently, large-scale energetic outflows from active galactic nucleus (AGN) have been invoked as a route to explain many of the properties of local massive galaxies. If post-starbursts are late-time mergers they may have passed through their quasar phase and, as a result, the AGN may provide sufficient energy to inhibit and terminate star formation (Bower et al. 2006). Indeed, post-starburst galaxies have been suggested as ideal laboratories for testing AGN feedback models (Tremonti, Moustakas & Diamond-Stanic 2007), and some observations indicate that such a link exists (Yan et al. 2006; Georgakakis et al. 2008). Finally, in dense environments (such as clusters) galaxy harassment and/or interaction with the hot intracluster gas is also likely a driving factor (Dressler & Gunn 1983; Pracy, Couch & Kuntschner 2010).

While high-resolution imaging has demonstrated that most bright, nearby E+A galaxies are spheroidal, often with signs of interaction (Yang et al. 2004; Balogh et al. 2005), their dynamics provide better constraints on their likely origins. Norton et al. (2001) obtained long-slit spectra of 20 E+A galaxies and used the ratio of the rotational velocity to linewidth to conclude that most of the galaxies are in the process of transforming from rotationally supported, gas-rich galaxies to pressure-supported, gas-poor galaxies. However, long-slit spectroscopy mixes spatial and spectral resolution, and a better understanding of the dynamics can be obtained from integral field spectroscopy, where the spatial and spectral information can be cleanly decoupled. This technique also allows the location, spatial extent and separation of any gas, old (K) stars and (the short-lived) massive A stars to be compared.

An example of such measurements was made by Swinbank et al. (2005) using the Gemini Multi-Object Spectrograph Integral Field Unit (GMOS-IFU) to map the properties of a H $\delta$  strong galaxy (SDSS J1013+0116) selected from the Sloan Digital Sky Survey (SDSS). In this galaxy, the velocity field and spatial extent of the distribution of H $\delta$  equivalent widths suggest that the post-starburst phase arose from a merger between a gas-rich spiral and a gas-poor, passive secondary. Crucially, within SDSS J1013+0116, the A stars are distributed throughout the galaxy, arguing that the starburst occurs in the disc of the galaxy during the interaction. The studies of Goto et al. (2008) and Pracy et al. (2009) increased the number of E+A galaxies with resolved spectroscopy to  $\sim 10$ , and showed that wide-spread A-star populations are a common feature, with A-star populations extended on  $\gg$  kpc scales. Pracy et al. (2009) also showed that the majority of their E+A galaxies have significant angular momentum per unit mass (so-called ‘fast rotators’), casting doubt on equal-mass, major mergers on the mechanism which results in E+A galaxies since these should leave dispersion-dominated kinematics.

In order to gain a better understanding of the interaction between star formation and gas dynamics within the interstellar medium (ISM) of E+A galaxies, we have obtained three-dimensional spec-

troscopy of 11 galaxies, selected from the SDSS in the redshift range  $0.07 < z < 0.12$ . The three-dimensional data are used to map the distribution and kinematics of A stars. We investigate the spatial distribution of residual star formation through the [O II]  $\lambda 3727$  emission and the distribution of the young A stars through the much stronger H $\delta$  absorption line. In Section 2 we present the data reduction and analysis. The results are presented in Section 3. Finally we summarize our results and present the implications in Section 4. We adopt a cosmology with  $\Omega_m = 0.27$ ,  $\Lambda = 1 - \Omega_m$  and a Hubble constant of  $72 \text{ km s}^{-1} \text{ Mpc}^{-1}$ . In this cosmology, at  $z = 0.09$  (the median redshift of our sample), 1 kpc subtends 0.6 arcsec on the sky.

## 2 OBSERVATIONS AND DATA REDUCTION

### 2.1 Sample selection

Our sample is selected from the catalogue of Balogh et al. (2005), which is based on *K*-band imaging of 222 nearby H $\delta$ -strong galaxies from Goto et al. (2003). This catalogue contains all galaxies for which the rest frame equivalent width of the H $\delta$  absorption line is  $W_o(\text{H}\delta) > 4 \text{ \AA}$  and  $W_o([\text{O II}]) < 10 \text{ \AA}$  (with  $>2\sigma$  confidence), as measured from the spectrum using a Gaussian profile fitting technique. Of these, we select galaxies which also have weak or absent H $\alpha$  emission,  $W_o(\text{H}\alpha) < 5 \text{ \AA}$ . This helps to exclude galaxies with weak or dusty star formation, as well as contribution from an AGN (Yan et al. 2006).

10 E+A galaxies from this sample were selected for follow-up IFU observations. These galaxies were selected to span different morphological types and environments. The former was quantified by fractional bulge luminosities (B/T) determined from the bulge-to-disc decompositions of Balogh et al. (2005), while the latter was obtained by cross-correlating with the C4 cluster catalogue (Miller et al. 2005). In practice, given our high mass cut, most of the candidates were bulge-dominated, as shown in fig. 4 of Balogh et al. (2005); we only found one clearly disc-dominated galaxy (J1048+0230, with B/T = 0.29). Furthermore, the vast majority of the E+A galaxies in Balogh et al. (2005) are not associated with clusters; we found only two galaxies satisfying our other selection criteria that are near clusters. In addition, we include J1013+0116 from Swinbank et al. (2005), to bring the final sample to 11 galaxies, as shown in Table 1. J1013+0116 was chosen for our pilot programme, for which we required reasonably strong line emission

**Table 1.** Target information. Coordinates, redshifts and exposure times of the galaxies in our sample. The two E+A galaxies labelled ‘\*\*’ (J0906+5221 and J1242+0237) are both in cluster environments. Note that J2013+0116 was selected to have weak emission lines, so is an e(a), rather than E+A, galaxy.

Target	$\alpha_{J2000}$ (h m s)	$\delta_{J2000}$ ( $^{\circ}$ ' '')	Redshift	Exp. time (ks)
J0835+4239	08 35 21.23	+42 39 36.0	0.0920	10.8
J0906+5221*	09 06 19.93	+52 21 50.0	0.0989	10.8
J0938+0001	09 38 42.91	+00 01 49.0	0.0914	18.0
J0948+0230	09 48 18.68	+02 30 04.1	0.0602	16.2
J1013+0116	10 13 45.39	+01 16 13.6	0.1055	10.8
J1242+0237*	12 42 52.96	+02 37 00.9	0.0846	10.4
J1348+0204	13 48 02.21	+02 04 05.6	0.0678	10.8
J1627+4800	16 27 55.98	+48 00 51.1	0.1254	13.0
J1642+4153	16 42 55.22	+41 53 35.5	0.0722	11.7
J1715+5822	17 15 46.24	+58 22 55.4	0.1271	15.6
J2307+1525	23 07 43.40	+15 25 59.3	0.0699	14.4

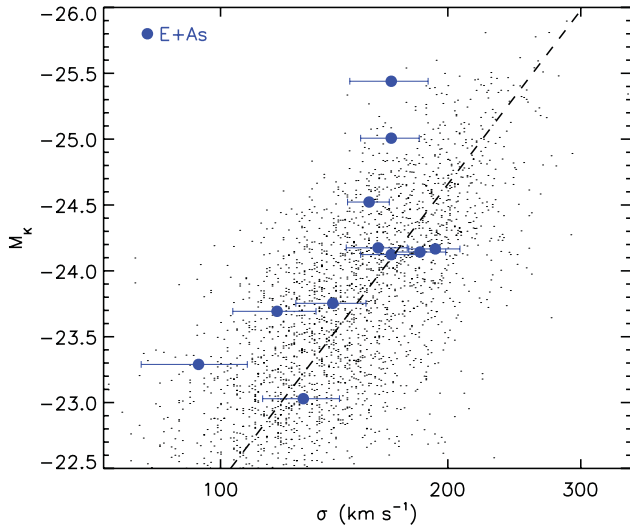


**Figure 1.** The  $K$ -band velocity–linewidth relation of the E+A galaxies in our sample compared to SDSS early-type galaxies from Bernardi et al. (2005), with  $K$ -band magnitudes taken from 2MASS. This figure shows that the E+A galaxies in our study span  $\sim 80$ – $180$   $\text{km s}^{-1}$  and  $\gtrsim 2$  mag in  $K$ . Our study focuses on the brighter E+A galaxies at a fixed velocity dispersion, due to the requirement of high signal-to-noise ratios to carry out this analysis.

to ensure reliable dynamical measurements could be made. Thus, it has the strongest [O II] emission in our sample ( $W_o[\text{O II}] = 5.2 \pm 0.3 \text{ \AA}$ ), and is more properly classified as an e(a) galaxy (Poggianti et al. 1999). This is therefore a fairly heterogeneous sample, by design.

In Fig. 1 we show where these galaxies lie in the luminosity–linewidth plane of the Faber–Jackson relation (Faber & Jackson 1976). We measure the velocity dispersions from the SDSS spectra, using the cross-correlation technique described in Section 2.2. We use the linewidth of the  $\text{Mg I}$  triplet as a proxy for the stellar kinematics of an old stellar population. The E+A galaxies in our sample span a range of velocity dispersions from  $\sigma \sim 80$  to  $180$   $\text{km s}^{-1}$ , and nearly two magnitudes in the  $K$  band. For comparison we also plot the early-type galaxies selected from SDSS (Bernardi et al. 2005), cross-matched to Two Micron All Sky Survey (2MASS). To ensure a fair comparison with the E+A galaxies, we limit the redshift range of the comparison sample to  $z < 0.1$ , and apply no  $k$ -corrections to either sample. As Fig. 1 shows, the E+A galaxies in our sample are systematically brighter in the  $K$  band for a fixed velocity dispersion ( $\Delta M_K = 0.6 \pm 0.2$ ). A comparable offset in  $R$  band ( $\Delta m_R \sim 0.6$  mag) was also noted by Norton et al. (2001) who used long-slit spectroscopy of 20 E+A galaxies from the sample described by Zabludoff et al. (1996).

The  $(u - g)$  versus  $(r - i)$  colours of the galaxies in our sample are shown in Fig. 2. We compare these to the galaxies from SDSS Data Release 5 (DR5) with redshift range  $0.05 < z < 0.1$  and magnitude range  $16 < r < 17$ . We also compute three evolutionary colour tracks: (i) an exponentially declining star formation rate (SFR), with  $\tau = 4$  Gyr, and  $\tau_v = 1$  mag extinction; (ii) a ‘truncated’ model which shows the colour evolution over a 2-Gyr period following truncation of star formation in the model; (iii) a model in which a 10 per cent (by mass) instantaneous burst is superposed upon the old stellar population. As Fig. 2 shows, this latter model provides the best match to the colours of our E+A galaxies, as shown in Balogh et al. (2005).

Finally, we note that of 10 galaxies in our sample that are covered as part of the VLA Faint Images of the Radio Sky at Twenty-

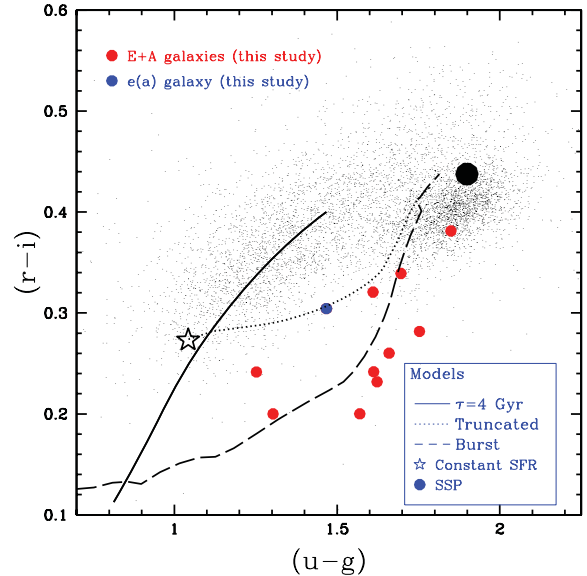


**Figure 2.** The observed  $(u - g)$  versus  $(r - i)$  distribution (corrected for Galactic reddening) of galaxies from the SDSS (model magnitudes). Small points represent a random subset of galaxies from DR5 with  $16 < r < 17$  in this redshift range; the bimodal nature of the population is evident. Filled, coloured circles represent our GMOS IFU targets; the red points are the E+A galaxies and the blue point is the single e(a) galaxy from Swinbank et al. (2005). The lines are the predictions of Bruzual & Charlot (2003) models, similar to those used in Balogh et al. (2005). All assume a Salpeter IMF and represent observed colours at  $z = 0.09$ . The filled, black circle represents an old population, resulting from a single burst of star formation 13.7 Gyr ago, while the star indicates the colour of a galaxy that has undergone constant star formation for the same amount of time, and includes internal extinction of  $\tau_v = 1$  mag. The solid line represents the track of an exponentially declining SFR, with  $\tau = 4$  Gyr, and  $\tau_v = 1$  mag extinction. The dotted line is a ‘truncated’ model, which shows the colour evolution over a 2-Gyr period following truncation of star formation in the model represented by the open star. Finally, the long-dashed line represents a model in which a 10 per cent (by mass) instantaneous burst is superposed upon the old stellar population (filled circle); the evolution from blue to red is followed for 2 Gyr following the burst. This latter model (which includes  $\tau_v = 1$  mag extinction) provides a reasonable match to the colours of our E+A galaxies, as shown in Balogh et al. (2005).

cm (FIRST) survey, two are detected at  $> 5\sigma$  (J0948+0230 and J1013+0116) and two more are detected at  $3\sigma$ – $5\sigma$  (0835+4239 and J1642+4153). These detections have 1.4-GHz fluxes in the range 0.5–2.2 mJy, corresponding to luminosities of  $L_{1.4} = 8$ – $15 \times 10^{21}$   $\text{W Hz}^{-1}$ . We return to this in Section 4.

## 2.2 GMOS spectroscopic imaging

Spectro-imaging observations of 10 new E+A galaxies in our sample were taken with the GMOS-North and GMOS-South IFU between 2005 and 2007 (Allington-Smith et al. 2002). Seven targets were observed in ‘stare’ mode using one-slit mode which results in a field of view of  $5 \times 7$  arcsec<sup>2</sup>, while four targets were observed with nod-and-shuffle in two-slit mode (resulting in a field of  $5 \times 5$  arcsec<sup>2</sup>). For observations taken with nod-and-shuffle we chopped away from the target by 30 arcsec every 30 s (see Swinbank et al. 2005, for a detailed discussion of the observing procedure). The exposure times for each target were typically 11–18 ks, with longer exposures taken on fainter targets (Table 1). All observations were carried out in dark time, typically with 0.6-arcsec seeing in  $V$  band

and in photometric conditions. The corresponding physical resolution is  $\sim 1.0$  kpc at the median redshift of our sample. We used the *B*-band filter in conjunction with the B600 or B1200 grating, which results in a spectral resolution of  $\lambda/\Delta\lambda \sim 2000$ – $4000$ .

The GMOS data reduction pipeline was used to extract and wavelength-calibrate the spectra of each IFU element. The variations in fibre-to-fibre response were removed using twilight flat-fields, and the wavelength calibration was achieved using a CuAr arc lamp. We also applied additional steps to improve the flattening and wavelength calibration using a series of custom IDL routines. The wavelength coverage of the final data is typically 3900–5500 Å, but varies depending on exact instrumental setup. Flux calibration was carried out using observations of standard stars through the IFU using identical setups as the target observations. From the observations of the standard star, we note that the amplitude of the point spread function (PSF) varies by  $<0.05$  arcsec across the wavelength range 4000–7000 Å and so the results in the following sections are insensitive to variations in PSF with wavelength (0.05 arcsec is  $\sim 1/4$  of the size of a lenslet).

Since the data cubes have a large wavelength coverage we correct for the parallactic angle in each cube by modelling a 3-hour observation running from  $-1$  to  $+1$  h angle with the corresponding minimum and maximum airmasses. After building the data cube, we model and correct this aberration using a linear interpolation at each slice of the data cube along the wavelength axis. We note that the typical airmass of these observations was  $\sim 1.2$  and the typical amplitude of the parallactic angle is  $\lesssim 0.3$  arcsec across entire wavelength range of each cube.

### 3 ANALYSIS

#### 3.1 Stellar masses and morphologies

Before discussing the spatially resolved properties, we first make use of the existing imaging to estimate the stellar masses and morphologies of the galaxies in our sample. To estimate the stellar masses, we follow McGee et al. (2011) and use spectral energy distribution modelling employing the Sloan *ugriz*- and *K*-band photometry (Balogh et al. 2005). Briefly, we generate galaxy templates using Bruzual & Charlot (2003) models with a Salpeter initial mass function (IMF; Salpeter 1955) assuming a lower and upper IMF mass cut-off of 0.1 and  $100 M_{\odot}$ , respectively. We follow the galaxy

parameter ranges used by Salim et al. (2007). The model spectra include a range of galaxy age (0.1–13 Gyr), metallicity ( $0.005$ – $2.5 Z_{\odot}$ ), star formation history and dust obscuration ( $A_V = 0$ – $6$  mag). In particular, the exponentially declining SFRs with superimposed bursts are randomly chosen with a uniform distribution, and we allow bursts that last some time randomly distributed in duration between 30 and 300 Myr. The strength of the bursts are also randomly chosen so that during the lifetime of the burst they produce between 0.03 and 4 times the stellar mass the galaxy had at the onset of the burst. From these model star formation histories, we generate magnitudes by convolving the resulting spectra with the *ugriz* and *K*-band filter response curves. To fit to the observations, we search the entire parameter space and minimize the  $\chi^2$ , but generate a probability distribution function for each parameter for each galaxy (see McGee et al. 2011, for a detailed discussion). The resulting stellar masses (and their  $1\sigma$  errors) are given in Table 2. The median stellar mass of the galaxies in our sample is  $8 \pm 2 \times 10^{10} M_{\odot}$ .

Since the *K*-band luminosity is a good tracer of the stellar mass (and is less sensitive to the recent star formation history than the optical bands), we can also perform a simple check of the stellar mass using a canonical mass-to-light ratio. Balogh et al. (2005) (see also Fig. 2) show that the  $(u - g)$  and  $(r - i)$  colours of E+A galaxies are consistent with a truncated star formation model in which a burst of 5–15 per cent is superimposed on to an old population, and use this to derive a canonical  $M/L_K = 0.8 \pm 0.1$ . Applying this to our *K*-band magnitudes, we derive  $M_* = 9 \pm 2 \times 10^{10} M_{\odot}$ , which is consistent with the estimates from the more sophisticated modelling above. This stellar mass is also comparable to the average stellar mass of the parent sample from Balogh et al. (2005):  $M_* = 8 \pm 2 \times 10^{10} M_{\odot}$ .

The SDSS imaging is also useful for measuring Sérsic indices, asymmetries and radial colour gradients within the galaxies which, along with the distribution of H $\delta$  equivalent widths, may provide a diagnostic of the physical mechanism(s) of E+A formation. For example, positive colour gradients (i.e. bluer in centre) can arise when young stars are more concentrated than the old stellar population. In this case, the distribution of H $\delta$  equivalent widths are also likely to be compact. In contrast, a negative colour gradient, together with a positive H $\delta$  equivalent width radial gradient, may represent a galaxy in which the molecular clouds are not confined to the nuclear regions.

**Table 2.** Properties of the E+A galaxies in our sample.

	Equivalent width		B/T	Sérsic	$M_*$	[O II] flux	SFR([O II])	$v \sin(i)/\sigma$	inc ( <i>i</i> )	$v_c$	$\lambda_R$	$r(\text{H}\delta)$	$A_{\text{H}\delta} > 6 \text{ \AA}$
	[O II]	H $\delta$		index	( $\times 10^{10}$ )	( $\times 10^{-16}$ )	( $M_{\odot} \text{ yr}^{-1}$ )		( $^{\circ}$ )	( $\text{km s}^{-1}$ )		(kpc)	( $\text{kpc}^2$ )
	(Å)	(Å)		( <i>n</i> )	( $M_{\odot}$ )	( $\text{erg s}^{-1} \text{ cm}^{-2}$ )							
J0835+4239	$2.9 \pm 0.2$	$6.9 \pm 0.3$	0.48	$7 \pm 1$	$8.3^{+2.6}_{-1.9}$	$5.0 \pm 0.5$	$0.14 \pm 0.07$	$0.4 \pm 0.1$	$51 \pm 11$	$55 \pm 15$	$0.11 \pm 0.04$	$2.4 \pm 0.2$	15.2
J0906+5221*	$1.5 \pm 0.3$	$6.3 \pm 0.4$	0.69	$4 \pm 1$	$2.0^{+0.5}_{-0.3}$	$2.3 \pm 1.0$	$0.08 \pm 0.04$	$1.0 \pm 0.1$	$26 \pm 5$	$75 \pm 12$	$0.27 \pm 0.04$	$2.0 \pm 0.2$	11.4
J0938+0001	$3.9 \pm 0.4$	$5.0 \pm 0.3$	0.47	$3.5 \pm 1.0$	$23.4 \pm 6.0$	$5.1 \pm 0.5$	$0.15 \pm 0.04$	$5.5 \pm 0.1$	$57 \pm 6$	$202 \pm 12$	$0.67 \pm 0.05$	$1.2 \pm 0.5$	$>0.8$
J0948+0230	$2.4 \pm 0.5$	$6.4 \pm 0.2$	0.29	$2.2 \pm 0.3$	$6.6^{+1.7}_{-1.2}$	$3.8 \pm 0.9$	$0.05 \pm 0.03$	$1.8 \pm 0.1$	$54 \pm 7$	$200 \pm 10$	$0.53 \pm 0.03$	$1.2 \pm 0.4$	$>0.8$
J1013+0116	$5.2 \pm 0.3$	$6.8 \pm 0.5$	0.46	$>7$	$15.0^{+7.2}_{-2.8}$	$12.1 \pm 0.2$	$0.48 \pm 0.12$	$0.2 \pm 0.1$	$42 \pm 10$	$152 \pm 14$	$0.27 \pm 0.04$	$2.8 \pm 0.3$	14.4
J1242+0237*	$2.0 \pm 0.4$	$6.0 \pm 0.2$	0.40	$3.8 \pm 0.5$	$1.9^{+0.5}_{-0.2}$	$2.7 \pm 0.6$	$0.06 \pm 0.03$	$0.5 \pm 0.1$	$21 \pm 5$	$92 \pm 6$	$0.20 \pm 0.03$	$1.0 \pm 0.2$	2.1
J1348+0204	$2.1 \pm 0.5$	$6.0 \pm 0.3$	0.67	$6.2 \pm 0.4$	$6.9^{+1.6}_{-1.3}$	$7.1 \pm 0.8$	$0.11 \pm 0.03$	$0.4 \pm 0.1$	$49 \pm 7$	$63 \pm 8$	$0.10 \pm 0.04$	$1.6 \pm 0.2$	2.2
J1627+4800	$0.8 \pm 0.4$	$5.2 \pm 0.5$	0.73	$>7$	$5.7^{+1.5}_{-1.2}$	$<2.1$	$<0.13$	$2.2 \pm 0.1$	$37 \pm 5$	$229 \pm 12$	$0.52 \pm 0.05$	$2.1 \pm 0.5$	4.4
J1642+4153	$1.2 \pm 0.5$	$6.5 \pm 0.5$	0.64	$3.5 \pm 0.6$	$6.0^{+1.7}_{-1.1}$	$4.5 \pm 1.0$	$0.08 \pm 0.03$	$1.2 \pm 0.1$	$51 \pm 6$	$201 \pm 10$	$0.41 \pm 0.04$	$1.5 \pm 0.3$	3.2
J1715+5822	$2.2 \pm 0.4$	$6.5 \pm 0.8$	0.48	$4.5 \pm 1.0$	$7.9^{+2.5}_{-1.9}$	$2.8 \pm 0.5$	$0.17 \pm 0.05$	$0.4 \pm 0.1$	$49 \pm 5$	$90 \pm 5$	$0.46 \pm 0.03$	$2.7 \pm 0.3$	6.5
J2307+1525	$1.7 \pm 0.3$	$6.3 \pm 0.4$	0.45	$>7$	$4.5^{+1.3}_{-0.9}$	$3.0 \pm 0.5$	$0.05 \pm 0.02$	$0.7 \pm 0.1$	–	–	$0.22 \pm 0.03$	$1.4 \pm 0.2$	2.8

*Notes.* The two E+A galaxies labelled \*\* (J0906+5221 and J1242+0237) are both in cluster environments. *n* denotes the Sérsic index measured from the SDSS *gri* photometry. The estimate of the SFR is calculated using the [O II] $\lambda 3727$  emission line flux and assuming the calibration from Kennicutt (1998).



From our sample of 11 galaxies, three show positive colour gradients [ $\Delta(g - i)/\Delta \log r > 0.0$ ], and the rest are either flat or mildly negative (see also Fig. 5 and Yang et al. 2008). The galaxies with bluer nuclei (positive colour gradients) may evolve into the negative gradients typical in E/SOs if the central parts of these galaxies are metal-enhanced (Yang et al. 2008). Finally, we note that the median asymmetry and Sérsic index of the sample is  $0.03 \pm 0.01$  and  $4.9 \pm 1.3$  respectively, characteristic of bulge-dominated systems.

### 3.2 Spatial distributions

To investigate the spatial distribution of the gas and stars in the galaxies, first we extract narrow-band slices from the data cube around the emission and absorption lines of interest. For a given emission or absorption line, we fit and subtract the continuum using a region  $\pm 100 \text{ \AA}$  from the centre of the emission or absorption feature using a  $3\sigma$  clip in the fit to be sure that neighbouring emission and absorption lines are omitted. We also extract continuum images from the data cube. For each image, we median filter each spectral pixel in the data cube between  $4350$  and  $4750 \text{ \AA}$  (rest frame) as a proxy for the ‘old’ stellar population (above the  $4000\text{-\AA}$  break) and between  $3650$  and  $3850 \text{ \AA}$  (rest frame) as a proxy for the ‘young’ stellar population and show these in the second row of Fig. 3. We caution that the continuum emission from above and below the  $4000\text{-\AA}$  break has contributions from both ‘old’ and ‘young’ stars. For example, for a 10 per cent by mass starburst which

has been truncated at 1 Gyr, for solar metallicity the contributions to the continuum emission from the burst to the total  $3650\text{--}3850$  and  $4350\text{--}4750 \text{ \AA}$  continuum emission are  $\sim 60$  and  $40$  per cent respectively, but can vary from 40 to 70 per cent in each band depending on starburst age and metallicity (Maraston 1998).

A better test of how the A stars are related to the underlying stellar emission (as well as the current star formation activity) is to turn to the  $H\delta$  absorption line. We estimate the equivalent width of  $H\delta$  at each spatial pixel following Balogh et al. (1999) (see also Goto et al. 2003). We first average each spatial pixel over a  $0.6 \times 0.6 \text{ arcsec}^2$  region to approximately match the seeing, and estimate the continuum flux using  $3\sigma$  clipped linear interpolation between two wavelength windows placed at either side of the  $H\delta$  line ( $4030\text{--}4082$  and  $4122\text{--}4170 \text{ \AA}$ ; Goto et al. 2003). This  $3 \times 3$  averaging produces an effective seeing disc of  $0.85 \text{ arcsec}$ , and this is taken into account in all of the following calculations. The rest-frame equivalent width of the  $H\delta$  absorption line is then calculated by summing the ratio of the flux in each pixel of the spectrum, over the estimated continuum flux in that pixel based on our linear interpolation; its distribution over the area of each galaxy is shown in Fig. 4. In this figure we also indicate the centroids of the nebular emission and continuum from above the  $4000\text{-\AA}$  break, with a  $1\sigma$  error ellipse. To calculate these error ellipses we compute the number of photons per pixel with their associated  $\sqrt{n}$  uncertainties, and recompute centroid with  $10^4$  Monte Carlo realizations. It is interesting to note that the regions of strongest  $H\delta$  absorption do not always coincide

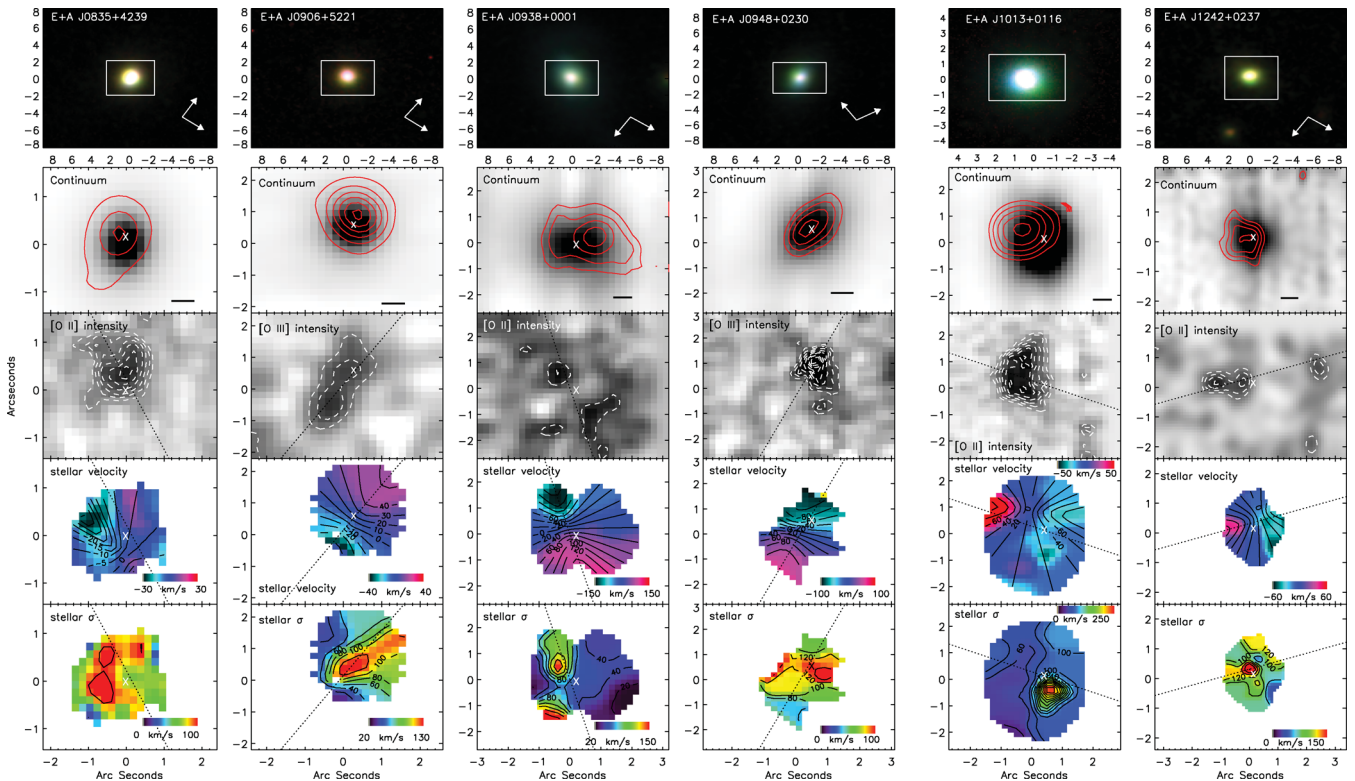


**Figure 3.** Results from the IFU observations of the E+A galaxies in our sample. From top to bottom: (1) true colour *BIK*-band images of each of the galaxies constructed from Gemini/GMOS imaging (blue), SDSS *i*-band (green) and UKIRT/UFTI *K*-band imaging (red). In each panel we overlay the GMOS IFU field of view. The arrows denote the directions of north and east. (2) Continuum images from the continuum above the  $4000\text{-\AA}$  break, derived by collapsing the data cube between  $4350$  and  $4750 \text{ \AA}$  in the rest frame, with dark grey indicating high intensity. The contours trace the continuum from the rest-frame  $3650\text{--}3850 \text{ \AA}$  continuum emission (which should have a stronger contribution from young stars than the continuum emission above the  $4000\text{-\AA}$  break). The solid bar in each panel denotes the seeing disc for the observations. (3) Gas phase emission line intensity (derived from either  $[O II] \lambda 3727$  or  $[O III] \lambda 5007$ , as indicated). The contours start at  $3\sigma$  and are incremented by  $1\sigma$ . (4) Two-dimensional stellar velocity fields of the galaxies, measured from the  $H\delta$  line. (5) Two-dimensional stellar velocity dispersion maps. The dotted line marks the major kinematic axis in the velocity fields, where it can be clearly identified.

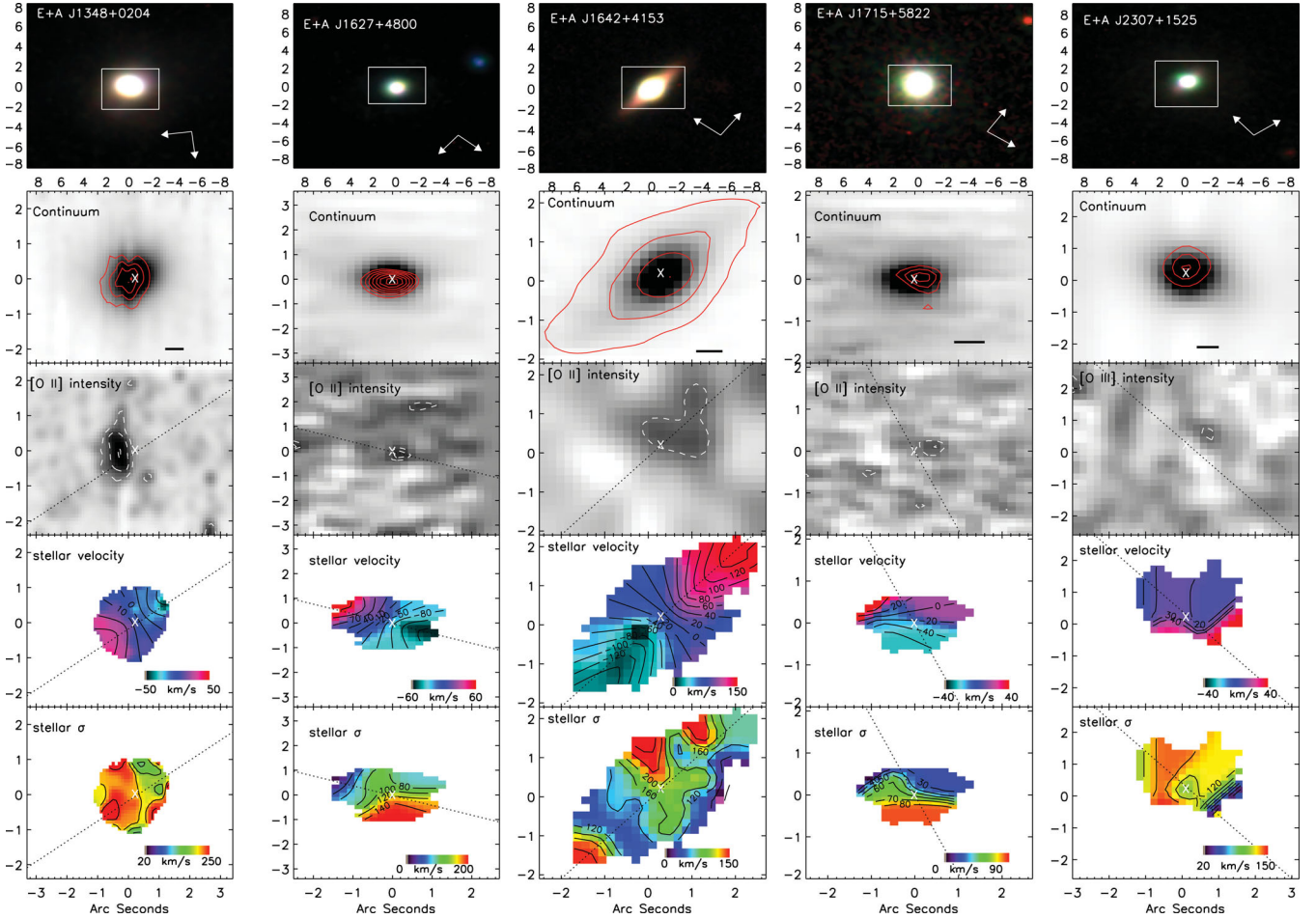
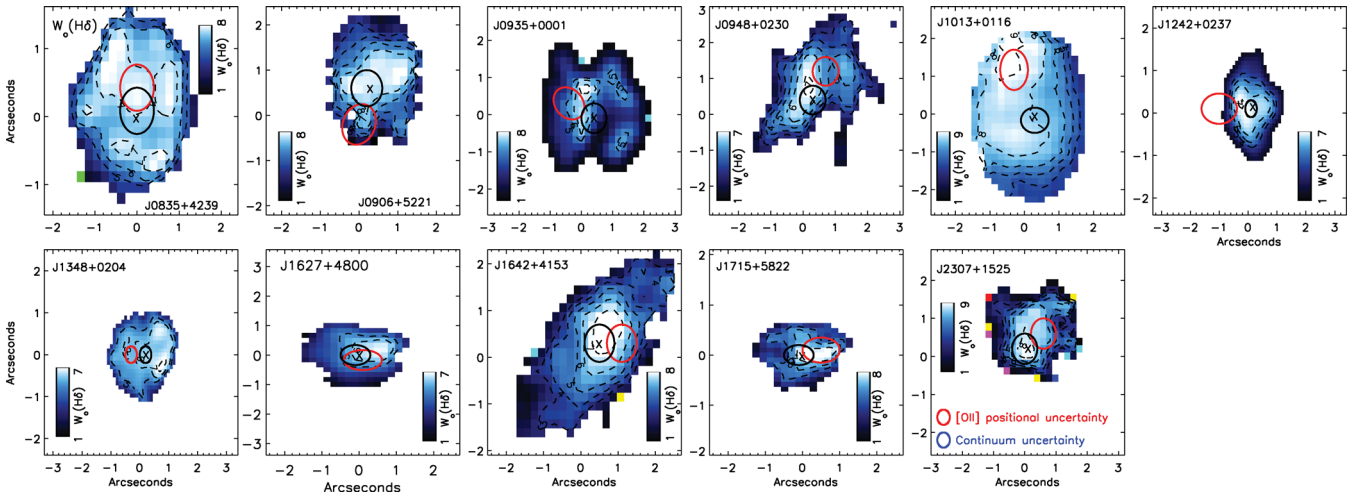
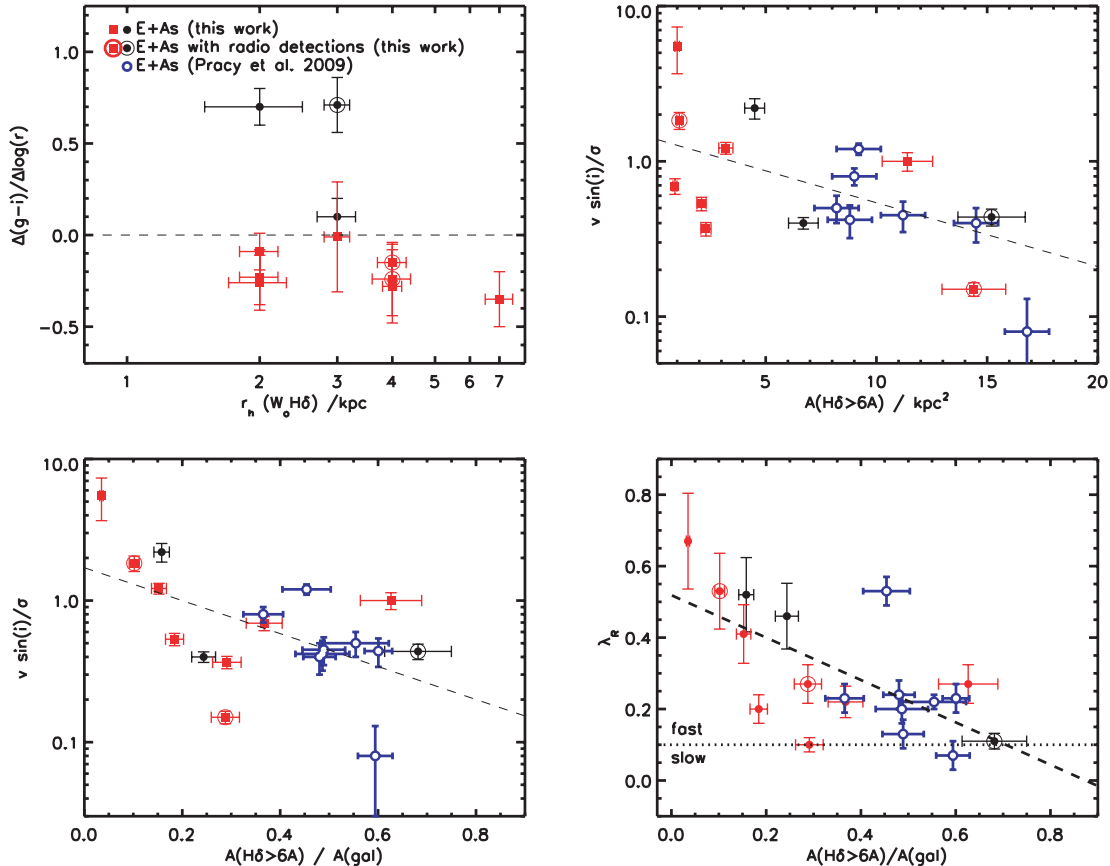


Figure 3. continued



**Figure 4.** The distribution of rest-frame H $\delta$  equivalent widths across each of the galaxies in our sample. The contours are separated by  $\Delta W_o(\text{H}\delta) = 1 \text{ \AA}$ . The ‘X’ denotes the centre of the galaxy as defined from the centre of the continuum above the 4000- $\text{\AA}$  break, while the ellipses denote the centre and  $1\sigma$  uncertainty in the nebular emission centroid (red) and continuum emission centroid (black). This figure highlights that six E+A galaxies in our sample have H $\delta$  absorption, nebular emission and continuum emission which are spatially co-located on  $\sim\text{kpc}$  scales (J0948, J1642, J1627, J1715, J2307), whilst three systems have significant offsets between nebular emission and H $\delta$  (J0906, J1242, J1348). Two galaxies have nebular emission and H $\delta$  in agreement, but with very extended H $\delta$  and nebular emission which is offset from the strongest continuum (J0835, J1013), suggesting that the A and OB stars formed in a different location than the older stars. At least in some cases, the new OB stars are either displaced from the older A stars. This reconciles the fact that both emission and strong absorption can be seen in the same, integrated galaxy spectrum – the two populations do not generally arise from exactly the same place.



**Figure 5.** The spatial extent of the A stars within the E+A galaxies in our sample as a function of colour gradient and kinematics. Top-left panel: the extent of the A stars (defined as the radius at which the H $\delta$  equivalent width drops to half the peak value along the major kinematic axis) as a function of the  $g - i$  colour gradient within the central 2 kpc of the galaxy. Positive radial colour gradients denote light that is bluer in the centre. The dashed line denotes a colour gradient of zero, and we use this to differentiate galaxies with positive (black filled circles) from negative colour gradients (red filled squares). In all panels, we identify the E+A galaxies which have weak radio emission ( $L_{1.4} \gtrsim 10^{22} \text{ W Hz}^{-1}$ ; highlighted with an open circle). Top-right panel: the spatial extent of the A stars as a function of the dynamics as measured from  $[v \sin(i)/\sigma]$  for the E+A galaxies in our sample. We also include the six E+A galaxies from Pracy et al. (2009). To provide a quantitative measure of the spatial extent of the A stars, we define  $A(H\delta > 6 \text{\AA})$  as the area over which the H $\delta$  is stronger than  $6 \text{\AA}$ . The galaxies with higher  $v \sin(i)/\sigma$  tentatively show signs of having more compact A-star distributions compared to galaxies which are pressure supported; the average  $v \sin(i)/\sigma$  for the galaxies where  $A(H\delta > 6 \text{\AA}) > 4 \text{ kpc}^2$  is  $0.5 \pm 0.2$ , compared with  $v \sin(i)/\sigma = 1.1 \pm 0.5$  for the others. Bottom-left panel: since the measurement of the spatial extent of H $\delta$  is sensitive to detecting the continuum, we normalize the area,  $A(H\delta)$ , by the spatial extent of the galaxy, as measured from the continuum above the  $4000\text{-\AA}$  break. We note that the results are insensitive to whether we use the SDSS  $r$ -band image to measure the half-light radius or  $R_e$ . This plot shows that the galaxies with the most compact H $\delta$  distribution tend to be those which have dynamics consistent with rotation, while the galaxies with A stars which are most widespread are those with dispersion-dominated dynamics. Bottom-right panel: the spatial extent of the A-star population normalized to the continuum as a function of  $\lambda_R$  (Emsellem et al. 2007). High and low  $\lambda_R$  correspond to ‘fast’ and ‘slow’ rotators, respectively. This plot shows that the fastest rotators tend to have the most compact A-star spatial distribution. We note that although our sample is small, the galaxies with weak AGN do not stand out in terms of their A-star extent or dynamics from the rest of the sample in any of the panels.

with regions with the strongest emission lines. Indeed, Fig. 4 shows that five objects have H $\delta$ , nebular emission and continuum emission which are spatially co-located on  $\sim \text{kpc}$  scales (J0948, J1642, J1627, J1715, J2307), whilst three systems have significant offsets between nebular emission and H $\delta$  (J0906, J1242, J1348). Two galaxies have nebular emission and H $\delta$  in agreement, but with very extended H $\delta$  which is offset from the strongest continuum (J0835, J1013). Thus, approximately half the sample are (relatively) simple in their A-star/gas/continuum emission, whilst half are clearly more complex. On average, the centroid of the A stars and the continuum emission are separated by  $\Delta r_{H\delta\text{-stars}} = 0.8 \pm 0.4 \text{ kpc}$ , whilst the average offset between the H $\delta$  and nebular emission is  $\Delta r_{H\delta\text{-gas}} = 1.0 \pm 0.2 \text{ kpc}$ , but can be as large as  $1.7 \text{ kpc}$ . This suggests that at least in some cases, the new OB stars are either displaced from the older A stars, or that the extinction is not uniform. In either case,

this helps to reconcile the fact that both emission and strong absorption can be seen in the same, integrated galaxy spectrum. The two populations do not generally arise from exactly the same place.

Next, we examine the spatial extent of the A stars through the H $\delta$  absorption. In the following calculations, we assume that the continuum emission is smoothly distributed and subtract the amplitude of the PSF at the redshift of the galaxy in quadrature from the areas covered by the continuum and A stars. As shown by the distributions in Fig. 4, the A stars are typically distributed over a large radius. We quantify this by computing the radius at which the H $\delta$  equivalent width drops to half the peak value (this is extracted along the major kinematic axes within the galaxy which is discussed in Section 3.3). This quantity,  $r_n(W_0 H\delta)$ , is compared with the observed  $g - i$  colour gradient within the central 2 kpc in the top-left panel of Fig. 5. Positive radial colour gradients



indicate galaxies that are bluer in the centre, and are measured in only three galaxies ( $\sim 30$  per cent). This is lower than the fraction of E+A galaxies with strong positive colour gradients (i.e. blue cores) found by Yamauchi & Goto (2005) ( $\sim 67$  per cent), but still higher than the fraction of early-type galaxies with positive colour gradients (Balcells & Peletier 1994). Within our sample, there is no evidence for the correlation between colour gradient and spatial extent of the A stars (as might have been expected from merger or tidal models for E+A formation; Bekki et al. 2005).

Another way to characterize the extent of the H $\delta$  absorption feature is to measure the area over which the equivalent width exceeds some threshold. We choose a threshold of  $6 \text{ \AA}$  and calculate the physical area  $A(H\delta > 6 \text{ \AA})$  for each galaxy. The results are shown in Fig. 5 as a function of various kinematic parameters, discussed below. Note that in all but one galaxy (J0948+0230) the area with  $W_o(H\delta) > 6 \text{ \AA}$  is significantly larger than the seeing. The median  $A(H\delta > 6 \text{ \AA}) = 4.0 \pm 2.1 \text{ kpc}^2$ , with a range of  $A(H\delta > 6 \text{ \AA}) = 0.8\text{--}15.2 \text{ kpc}^2$ . In comparison to the continuum emission from above the 4000- $\text{\AA}$  break, the A stars cover at least  $\sim 10$  per cent of the area, with a median of  $33 \pm 5$  per cent. Such widespread A-star populations have also been found in previous samples: Goto et al. (2008) show that the A stars in two SDSS-selected E+A galaxies are distributed over  $\sim 10 \text{ kpc}^2$ , while the seven E+A galaxies from Pracy et al. (2009) have A stars that are typically distributed over  $5\text{--}15 \text{ kpc}^2$ .

In summary, we note two important observations. First, the H $\delta$  is widespread, typically over  $A(H\delta > 6 \text{ \AA}) = 4.0 \pm 2.1 \text{ kpc}^2$  and thus the unusual spectrum characteristic of E+A galaxies is a property of the galaxy as a whole. It is not due to a heterogeneous mixture of populations, such as a nuclear starburst with a very high equivalent width ( $> 10 \text{ \AA}$ ) on top of an otherwise normal galaxy. Secondly, in approximately half of our sample, the A stars, nebular emission and continuum are not co-located, suggesting that the newest stars are often forming in a different place than those that formed  $\lesssim 1$  Gyr ago, and that recent star formation has occurred in regions distinct from the continuum emission (the older stellar populations).

### 3.3 Kinematics

To obtain the stellar velocity structure within the galaxies, we first construct a continuum image of the galaxy from the data cube collapsed between 4350 and 4750  $\text{\AA}$ , and bin the data to a constant signal-to-noise ratio per bin using the Voronoi binning method (Cappellari & Copin 2003). We demand a signal-to-noise ratio of 30 in continuum, and then cross-correlate each of the individual spatial regions with a library of template spectra (Vazdekis & Arimoto 1999). The cross-correlation is performed using the penalized pixel fitting method (PPXF; Cappellari & Emsellem 2004) and we derive the velocity field of the young stellar population using the wavelength range 3800–4290  $\text{\AA}$  which covers Ca, H & K and H $\delta$ .

As Fig. 3 shows, all 11 galaxies have velocity gradients in their dynamics, with amplitudes ranging from 30 to 200  $\text{km s}^{-1}$ . At least eight have dynamics that appear to be consistent with rotation, i.e. the peak of the line-of-sight velocity dispersion is at the dynamical centre, and the velocity field is characteristically bisymmetric, showing a so-called ‘spider’ diagram. For these galaxies, we model the velocity field in order to estimate the inclination and true rotational velocity. To achieve this, we use a simple approach and model the velocity field with an *arctan* function to describe the shape of the rotation curve such that  $v(r) = v_c \arctan(r/r_t)$ , where  $v_c$  is the asymptotic rotational velocity and  $r_t$  is the effective radius at which the rotation curve turns over (Courteau 1997). We then

construct a two-dimensional kinematic model with six free parameters ( $v_c$ ,  $r_t$ ,  $[x/y]$  centre, position angle and inclination) and use a genetic algorithm with  $10^5$  random initial values and a scalefactor of 0.95 to search for a best fit. We demand  $> 30$  generations are performed before testing for convergence to a solution, throwing out (a maximum of) 10 per cent of the solutions in each generation. The best-fitting kinematic maps are shown as contours in Fig. 3, and the best-fitting inclination and rotation speed are given in Table 2. Using the velocity maps and model fits, we identify the major kinematic axis wherever possible and extract the one-dimensional rotation curve and velocity dispersion profile along and show these in Fig. 6. From each of the two-dimensional maps, we also extract the distribution of H $\delta$  equivalent widths, both in radial bins and along the kinematic cross-section.

A measure of whether the dynamics are dominated by ordered- or random- motion can be obtained by measuring the ratio of rotational velocity to line-of-sight velocity dispersion,  $v \sin(i)/\sigma$ . We derive a median luminosity-weighted  $v \sin(i)/\sigma = 0.8 \pm 0.4$  for the whole sample with a range of 0.2–5.5. However, Fig. 7 shows that there is a weak correlation between absolute magnitude and  $v/\sigma$ , such that the lower luminosity systems have an increasing rotational support, although only four of the 11 galaxies have  $v/\sigma > 1$ , uncorrected for inclination. Recent studies of early-type galaxies from Emsellem et al. (2007) identify a comparably weak trend of  $v/\sigma$  with magnitude (although we note that their sample has a slightly lower average  $v/\sigma$  with an average  $v/\sigma = 0.30 \pm 0.03$ ). Indeed, the early types in Emsellem et al. (2007) have  $M_R = -21.8 \pm 0.3$  compared to  $M_R = -21.5 \pm 0.5$  for the E+A galaxies, and with stellar masses of  $1.0 \pm 0.3 \times 10^{11} M_\odot$ , which is also consistent with our sample. Thus, these early types and ellipticals from Emsellem et al. (2007) also have many of the properties expected for the descendant population of E+A galaxies.

Bender, Saglia & Gerhard (1994) also find a correlation between magnitude and  $v/\sigma$  for luminous elliptical galaxies. Although the Bender et al. (1994) sample is dominated by brighter galaxies than the E+A galaxies studied here (typically  $\sim 1.3$  mag brighter), those galaxies with high  $v/\sigma$  ( $\sim 1$  and so comparable to the E+A galaxies) are increasing dominated by lower mass, lower luminosity Sb–S0s.

A better test of the dynamical state of galaxies with low  $v/\sigma$  can be made by measuring the luminosity-weighted stellar angular momentum per unit mass,  $\lambda_R$ , as developed by Emsellem et al. (2007). This combines the velocity amplitude and line-of-sight velocity dispersion:  $\lambda_R = \langle R|v| \rangle / (R\sqrt{v^2 + \sigma^2})$ , where  $R$ ,  $v$  and  $\sigma$  are the radius, rotational velocity and velocity dispersion from the kinematic centre.  $\lambda_R$  is designed to quantitatively distinguish galaxies that have similar  $v/\sigma$  values but very different velocity structures by identifying those galaxies with significant angular momentum per unit mass. Emsellem et al. (2007) define ‘fast’ and ‘slow’ rotators as  $\lambda_R > 0.10$  and  $\lambda_R < 0.10$ , respectively. Classically, ‘fast’ rotators are dominated by low-mass spheroids (with a large  $v/\sigma$ ) whilst ‘slow’ rotators are dominated by ellipticals, albeit with a large range in  $M_R$ . We report  $\lambda_R$  for each galaxy in Table 2. Our sample has a median  $\lambda_R = 0.35 \pm 0.1$ , and all of the galaxies in our sample have  $\lambda_R > 0.1$ . When including the E+A galaxies from Pracy et al. (2009), 18/19 galaxies with well-resolved dynamical maps have  $\lambda_R > 0.1$ . Taken with the measurements of  $v/\sigma$ ,  $\lambda_R$  and stellar masses, the E+A galaxies in our sample have properties comparable to those measured in local, representative elliptical galaxies and S0s where similar measurements have been made.

To investigate how the dynamics and A star populations are related, we correlate the kinematics as measured from  $v/\sigma$  and  $\lambda_R$  as



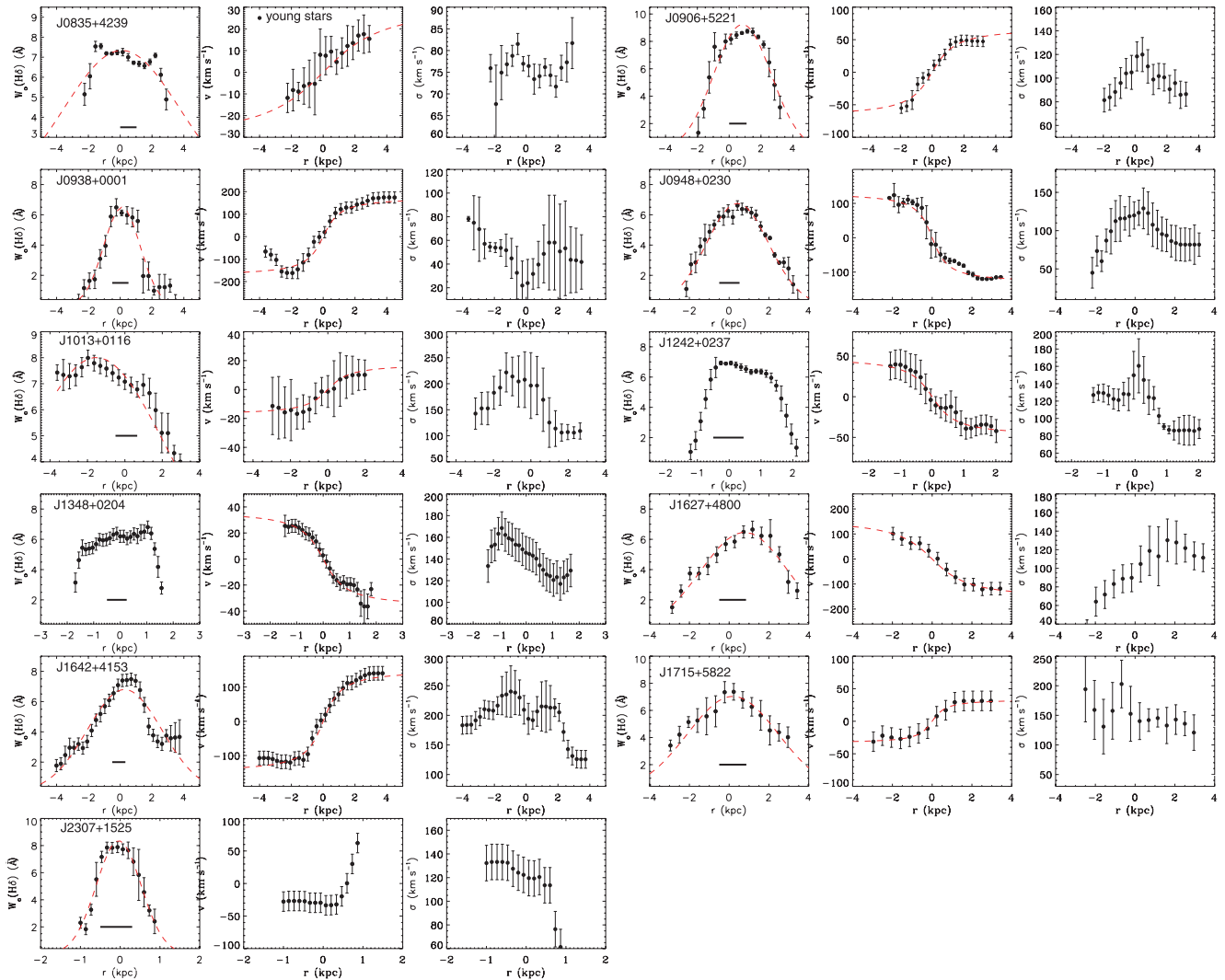


**Figure 6.** Extracted, one-dimensional equivalent width, velocity and line-of-sight velocity dispersion profiles are shown for each of the E+A galaxies in our sample. The profiles are extracted along the major axis as indicated in Fig. 3. Left: one-dimensional extent of equivalent widths. Middle: one-dimensional rotation curve of the galaxy with the best-fit rotational model (where appropriate) overlaid as contours. Right: one-dimensional distribution of linewidths. The solid bar in the left-hand panel denotes the amplitude of the seeing disc, converted to physical scale at the redshift of each galaxy.

a function of the A-star spatial extent and colour gradients. Fig. 5 shows that the galaxies which have the highest  $v/\sigma$  also have the most compact A-star distributions. Indeed, the average  $v/\sigma$  for the galaxies where  $A(\text{H}\delta > 6 \text{ \AA}) > 4 \text{ kpc}^2$  is  $0.5 \pm 0.2$ , compared with  $v/\sigma = 1.1 \pm 0.5$  for the remainder. We note that we would expect the opposite correlation between the spatial extent of the A stars and  $v/\sigma$  if the measurements were being driven by signal-to-noise ratio effects alone (low  $v/\sigma$  values would be expected for the most compact sources where it is more difficult to identify large velocity gradients). However, measuring the spatial extent of H $\delta$  absorption is sensitive to detecting the continuum, so we also normalize the area with  $A(\text{H}\delta > 6 \text{ \AA})$  by the spatial extent of the continuum emission,  $A(\text{gal})$ , as measured from the continuum. For the continuum measurement, we use the flux redwards of the 4000- $\text{\AA}$  break as measured from our IFU observations, although we note that the results are quantitatively similar when using the  $r$ -band half-light radius, or  $R_e$ , measured from SDSS imaging. In all panels, we find that galaxies with high  $v/\sigma$  show the most compact A-star populations.

Of course, the spatial distribution of an equivalent width depends on its intrinsic spatial distribution as well as the overall distribution of the continuum light (or galaxy surface brightness profile) after convolving with the seeing (e.g. Pracy et al. 2005). In particular, for a galaxy with a centrally concentrated equivalent width profile, the steeper the continuum surface brightness profile, the more the stellar population in the galaxy centre will contaminate the outer regions after convolution with the seeing (see Pracy et al. 2010, for a detailed discussion). In principle, this could give a correlation between  $v/\sigma$  and the extent of the A-star light distribution. Whilst full modelling to recover the intrinsic equivalent width distribution is beyond the scope of this paper, we can perform a simple test of whether this effect is likely to significantly contribute our results. We therefore construct  $10^4$  mock GMOS data cubes with variable amplitude velocity fields, continuum emission and H $\delta$  equivalent width profiles (which broadly bracket the range of our observations) and convolve these with the seeing. We note that in these simulations, the extent of the continuum emission and H $\delta$  profiles are independent. We measure the ‘true’  $v/\sigma$  and ratio of  $A(\text{H}\delta > 6)/A(\text{gal})$  as well

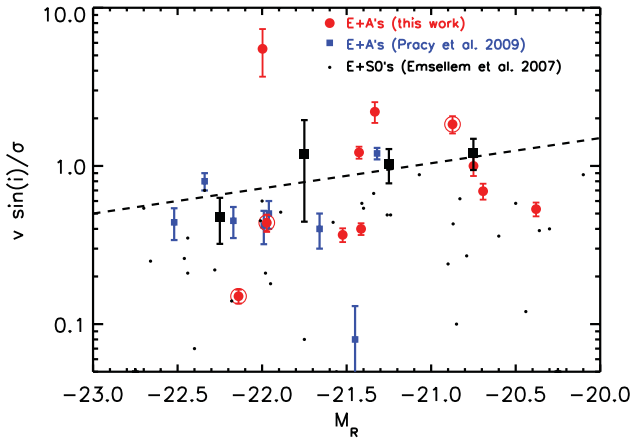


**Figure 7.** The dynamical measurement of  $v \sin(i)/\sigma$  as a function of absolute  $R$ -band magnitude for E+A galaxies from our sample and the recent work by Pracy et al. (2009). The solid black points denote the average values in bins of  $\Delta m = 0.5$  and the dashed line shows a linear fit, indicating a weak trend such that fainter galaxies tend to have higher  $v \sin(i)/\sigma$ . The plot also includes a comparison to the early-type and elliptical galaxies from Emsellem et al. (2007) [we have colour-corrected their sample from  $M_B$  to  $M_R$  using a  $(B - R) = 2.0$  appropriate for an early-type galaxy at  $z = 0.05$ ]. This sample has a lower  $(v/\sigma)$ , with  $v \sin(i)/\sigma$  ( $0.30 \pm 0.03$ ), but shows a comparably weak trend of increasing absolute magnitude. Galaxies which are weak radio sources (and thus may harbour AGN are shown as open symbols) do not stand out from the rest of the sample.

as the same quantities from the recovered cubes after convolution with the seeing and surface brightness limits appropriate for our observations. Allowing the spatial extent of the A stars to vary from ‘unresolved’ to three times the continuum emission, we find that the change in slope of  $\Delta \log(v/\sigma)/\Delta[A(H\delta > 6)/A(\text{galaxy})]$  is  $-0.04$  to  $-0.2$  depending on choice of parameters. The gradient of the correlation seen in Fig. 5 is  $\Delta \log(v/\sigma)/\Delta[A(H\delta > 6)/A(\text{galaxy})] = -2.2 \pm 0.3$ . Thus the underlying A-star distribution, continuum surface brightness profile and seeing may contaminate the correlation between the extent of the A stars and dynamics seen in Fig. 5, but it seems unlikely that this effect alone can account for the correlation we see. We also note that, in general, rotation-dominated galaxies have shallower surface brightness profiles than pressure-supported galaxies (e.g. Courteau 1997). This means there is a physical correlation between the two which may lead to an indirect correlation between  $v/\sigma$  and  $A(H\delta)/A(\text{gal})$ . However, clearly, observations of a well-matched control sample of non-E+A galaxies around the  $H\delta$  are required to examine whether the correlation in Fig. 5 is a result of the processes which drive the E+A galaxies. Nevertheless, for our sample the ‘slow rotators’ tend to have the most widespread A-star populations, while the ‘fast rotators’ have the more compact A-star distributions.

#### 4 DISCUSSION

There are at least three important unresolved problems regarding E+A galaxies. (1) From where in the galaxy does the unusual spectrum originate? (2) What star formation history leads to the spectral characteristics of these galaxies? (3) What triggers the recent change in star formation history? To address these issues, we have performed three-dimensional spectroscopy of a sample of 11 massive E+A galaxies selected from the SDSS for their unusually strong  $H\delta$  equivalent widths but weak  $[O\text{II}]$  emission, suggesting

that star formation in these galaxies was recently truncated, possibly following a starburst.

Our sample was selected to span a range of morphology and environment and hence is diverse by design. Moreover, with a limited sample size of 11 galaxies it is not possible to answer any of these questions definitively, especially since there may be more than one way to form an E+A galaxy. Nevertheless, there are several important results that are generic within our sample. First, we note that we see no strong correlation of the galaxy dynamics with the  $K$ -band morphology, or the environment of the galaxy with their kinematics or morphology of the nebular emission or A stars: the two E+A galaxies in dense environments do not appear to stand out from the rest of the sample in any of their properties, so we discuss the properties of the ensemble below.

To investigate the likely age of the starbursts and hence star formation history, we estimate the age of the A-star populations by comparing the average galaxy spectrum for each galaxy with the spectral library of Jacoby, Hunter & Christian (1984). We use the strength of the Ca K3933 Å absorption line (which is especially sensitive to age; Rose 1985), together with the equivalent width of the Ca H3969 Å (and Hε) absorption lines. For all of the E+A galaxies in our sample, the spectra best resemble that of an  $A5 \pm 1$  star, with an effective temperature of 8160 K. Interpolating the theoretical isochrones from Bertelli et al. (1994), this suggests a luminosity-weighted age of  $0.8 \pm 0.1$  Gyr [for the main-sequence (MS) turn-off at A8] although we caution that stellar masses and metallicity make this estimate uncertain. Nevertheless, this is also supported by the broad-band colours which are well matched by a model in which an instantaneous starburst (which accounts for 10 per cent by mass) is superposed upon the continuum above the 4000-Å break (Fig. 2).

Thus, the colours and line strengths we observe can best be reproduced with  $\sim 10$  per cent (by mass) starbursts on top of an old population (e.g. Shioya, Bekki & Couch 2004; Balogh et al. 2005). It is also evident that any residual star formation in the galaxy is negligible: the median stellar mass of the E+A galaxies in our sample is  $8 \pm 2 \times 10^{10} M_{\odot}$ , suggesting an average burst mass of  $M_{\text{burst}} \sim 1.0 \times 10^{10} M_{\odot}$ . The median SFR of galaxies in our sample (including limits) is  $\text{SFR}([O\text{II}]) = 0.13 \pm 0.03 M_{\odot} \text{ yr}^{-1}$ , less than 2 per cent of the past average SFR. Thus, the presence of even moderately strong  $H\delta$  absorption ( $> 3 \text{ \AA}$  or so) indicates that the SFR at truncation was at least comparable to the past average rate. Integrating the current SFR over 1 Gyr we derive a mass of  $\sim 1 \times 10^8 M_{\odot}$ , or only  $\sim 0.1$  per cent of the total galaxy mass. Since the mass involved in the burst is at least  $\sim 10$  per cent of the mass of the stellar mass, this suggests that the main progenitors of our E+A galaxies had significantly higher SFRs than seen today, and were most likely blue-cloud, star-forming systems.

The A stars are widely distributed, with an average  $A(H\delta > 6 \text{ \AA}) = 4.0 \pm 2.0 \text{ kpc}^2$ , and a range of  $A(H\delta > 6 \text{ \AA}) = 0.8\text{--}15.2 \text{ kpc}^2$  (see also Swinbank et al. 2005; Goto et al. 2008; Pracy et al. 2009). On average, the strongest  $H\delta$  [ $W_o(H\delta) > 6 \text{ \AA}$ ] covers  $33 \pm 5$  per cent of the area defined by the detected continuum above the 4000-Å break. It is also interesting that none of our galaxies shows regions with very strong absorption,  $W_o(H\delta) > 10 \text{ \AA}$ , at least on  $\sim \text{kpc}$  scales. Such strong absorption would be an unambiguous indication of a significant *enhancement* of the SFR in the past  $\lesssim 1$  Gyr; weaker lines can be formed via truncation of star formation in normal, gas-rich galaxies (e.g. Balogh et al. 1999). Moreover, it is also clear that in approximately half of the sample, the A stars (which give rise to the absorption) and nebular emission are not co-located, suggesting that the newest stars are often forming in a different place

than those that formed  $\lesssim 1$  Gyr ago. Thus, together with the burst mass to stellar mass ratio, this suggests that there needs to have been a recent, dramatic change in star formation history, coordinated over kpc scales in these galaxies.

The galaxies display a range of kinematic properties: all 11 have velocity gradients in their stellar kinematics and we derive a median luminosity-weighted  $v \sin(i)/\sigma = 0.8 \pm 0.4$  for the whole sample (with a range of 0.2–5.5). Fig. 7 shows that there is a weak correlation between absolute magnitude and  $v/\sigma$ , such that the lower luminosity systems have an increasing rotational support. The median  $\lambda_R$  for the E+A galaxies in our sample is  $\lambda_R = 0.35 \pm 0.1$ , and all of the E+A galaxies studied here have  $\lambda_R > 0.1$ , which is consistent with that found for a comparably bright sample of elliptical galaxies and passive S0's which are also well matched in their average stellar masses (Emsellem et al. 2007).

Although we have shown that the E+A phase is a galaxy-wide phenomenon, conclusively addressing what triggers the E+A phase is more difficult, especially since there are a number of processes which could be responsible at once (e.g. strong interactions or mergers, possibly preceded by AGN activity). However, we can search for global trends in the A-star population with other galaxy properties in order to search for the major contributing factor. We find that dynamics are correlated with the spatial extent of the A stars such that the ‘slow rotators’ have the most widespread A-star populations, while the ‘fast rotators’ have compact A-star distributions. Since the E+A galaxies in our sample do not preferentially lie in dense/cluster environments, it is unlikely that any truncation of star formation was due to ram pressure stripping of the gas.

It is interesting to note that theoretical models which aim to trace the formation and evolution of early-type galaxies have shown that there are two primary factors which determine the structure of early-type galaxies. More anisotropic and slowly rotating galaxies result from predominantly collisionless major mergers, while faster rotating galaxies are produced by more gas-rich mergers, where dissipation plays an important role (Kormendy & Djorgovski 1989; Bender, Burstein & Faber 1992; Faber et al. 1997). The second major factor which drives the galaxy structure is the mass fraction of the merger components. Unequal-mass galaxy mergers tend to produce more rapidly rotating galaxies than mergers with comparable mass ratios (Naab, Burkert & Hernquist 1999; Naab & Burkert 2003). Whichever process was responsible, the encounter has left residual rotational motion in at least 90 per cent of our sample, with A stars widely distributed within the ISM. Qualitatively, our results are consistent with models of unequal-mass, gas-rich mergers.

Finally, it is interesting to examine whether activation of a central black hole could be related to the end of star formation (Yan et al. 2006). As described in Section 2.2, four of our galaxies are detected in FIRST with 1.4-GHz fluxes in the range 0.5–2.2 mJy, corresponding to luminosities of  $L_{1.4} = 8\text{--}15 \times 10^{21} \text{ W Hz}^{-1}$ . All four galaxies with FIRST detections show [O III] and (weaker) [O II] emission. For these galaxies, the centroid of the nebular emission appears offset from the continuum by 0.4–1 kpc, but this is consistent with the rest of the sample. Thus, if there is an AGN in these galaxies, it does not appear to be the sole contributor to the nebular emission. Moreover, if the radio emission were due to star formation, then the instantaneous SFR would be 6–11  $M_{\odot} \text{ yr}^{-1}$  (Helou, Soifer & Rowan-Robinson 1985) a factor  $\sim 60$  times that inferred from the nebular emission lines. This could be possible if the galaxies are exceptionally dusty, although this seems unlikely given the

blue ( $r - i$ ) colours; we would expect dusty, star-forming galaxies to lie on the upper edge of the blue cloud in Fig. 2, with  $(r - i) > 0.4$  (Wolf, Gray & Meisenheimer 2005; Balogh et al. 2009). Thus, it is most likely that the radio emission arises from an AGN. In all the key figures, we have highlighted the E+A galaxies in our sample that have  $L_{1.4} \gtrsim 10^{22} \text{ W Hz}^{-1}$ . In all cases, their properties appear to be consistent with those of the rest of the sample. Thus, although we only have small number statistics, our results suggest that AGN activity in E+A galaxies does not play a dramatic role in defining the spatial or kinematic properties of the A stars, and/or that its effects are short-lived.

## 5 CONCLUSIONS

We have investigated the spectrophotometric properties of a sample of 11 E+A galaxies in the redshift range  $0.12 < z < 0.07$  in order to provide constraints on the physical processes which cause the unusual post-starburst signatures. Although our sample selection was heterogeneous (by design we selected E+A galaxies with a range of morphologies and environments), there are several important results which can be summarized as follows.

(i) The strongest H $\delta$  ( $W_{\delta} > 6 \text{ \AA}$ ) tends to widely distributed within the galaxies, on average covering  $\sim 33$  per cent of the galaxy image and extending over areas of 1–15  $\text{kpc}^2$ . This suggests that the characteristic E+A signature is a property of the galaxy as a whole and not due to a heterogeneous mixture of stellar populations.

(ii) In approximately half of the sample, the A stars, nebular emission and continuum are not co-located. The average offset between the H $\delta$  and nebular emission is  $\Delta r_{\text{H}\delta\text{--gas}} = 1.0 \pm 0.2 \text{ kpc}$ , but can be as large as 1.7 kpc. This suggests that at least in some cases, the new OB stars are either displaced from the older A stars or that the extinction is not uniform. In either case, this helps to reconcile the fact that both emission and strong absorption can be seen in the same, integrated galaxy spectrum. The two populations do not generally arise from exactly the same place.

(iii) The colours and line strengths of these E+A galaxies are consistent with a  $\sim 10$  per cent (by mass) starburst on top of an old population suggesting an average burst mass of  $M_{\text{burst}} \sim 10^{10} M_{\odot}$ . The current (residual) star formation is unable to account for the burst mass. This indicates that the main progenitors of most of our E+A galaxies were blue-cloud, star-forming galaxies in which there was a recent, dramatic change in star formation history, coordinated over kpc scales.

(iv) The kinematics show that some level of rotation in the A-star population is common, and the dynamics ( $v/\sigma$  and  $\lambda_R$ ) are consistent with those measured in comparably bright early types recently studied by Emsellem et al. (2007), which are also well matched in their average stellar masses. Whichever process was responsible for causing the starburst and subsequent truncation, the encounter has left residual rotational motion in at least 90 per cent of the sample, with A stars widely distributed within the ISM.

(v) We find that the A-star dynamics are correlated with their spatial extent such that the ‘slow rotators’ have the most widespread A-star populations, while the ‘fast rotators’ have compact A-star distributions.

(vi) We also find that the fraction of galaxies which have radio emission suggestive of low luminosity AGN is 20–40 per cent, a factor  $\sim 8$  times higher than expected given their stellar masses, indicating a high AGN fraction of E+A galaxies. However, although our sample is limited to only 11 galaxies, the kinematics and spatial

distribution of the stars in the radio-detected subsample do not stand out from the radio-undetected systems, suggesting that AGN feedback in E+A galaxies does not play a dramatic role in defining their properties, and/or that its effects are short.

Whichever process was responsible for the E+A signatures, rotational motion is seen in the majority of our sample, and their dynamics, stellar masses and luminosities are consistent with those expected for the progenitor population of (at least a subset of) representative, early-type galaxies. Overall, these observations provide new and detailed constraints on the kinematics and spatial distribution of the A stars and gas in E+A galaxies, and hence constraints on galaxy formation models which aim to test the variety of physical mechanisms which trace the evolutionary sequence linking gas-rich, star-forming galaxies to quiescent spheroids.

## ACKNOWLEDGMENTS

We gratefully acknowledge the referee for constructive report which significantly improved the content and clarity of this paper. AMS acknowledges an STFC Advanced Fellowship. AIZ acknowledges funding from NASA ADAP grant NNX10AE88G and also thanks the Institute of Astronomy at Cambridge University and the Center for Cosmology and Particle Physics at New York University for their hospitality during the completion of this paper. We thank Dave Alexander, Alastair Edge and Russel Smith for numerous useful conversations. These observations are based on programmes GS-2005B-Q-15, GN-2005B-Q-17, GN-2006B-Q-46, GN-2007A-Q-27 and GS-2007A-Q-22 from observations obtained at the Gemini Observatory, which is operated by the Association of Universities for Research in Astronomy, Inc., under a cooperative agreement with the NSF on behalf of the Gemini partnership: the NSF (US), STFC (UK), the NRC (Canada), CONICYT (Chile), the ARC (Australia), CNPq (Brazil) and CONICET (Argentina).

## REFERENCES

- Allington-Smith J. et al., 2002, *PASP*, 114, 892  
 Balcells M., Peletier R. F., 1994, *AJ*, 107, 135  
 Balogh M. L., Morris S. L., Yee H. K. C., Carlberg R. G., Ellingson E., 1999, *ApJ*, 527, 54  
 Balogh M. L., Miller C., Nichol R., Zabludoff A., Goto T., 2005, *MNRAS*, 360, 587  
 Balogh M. L. et al., 2009, *MNRAS*, 398, 754  
 Bekki K., Couch W. J., Shioya Y., Vazdekis A., 2005, *MNRAS*, 359, 949  
 Bender R., Burstein D., Faber S. M., 1992, *ApJ*, 399, 462  
 Bender R., Saglia R. P., Gerhard O. E., 1994, *MNRAS*, 269, 785  
 Bernardi M., Sheth R. K., Nichol R. C., Schneider D. P., Brinkmann J., 2005, *AJ*, 129, 61  
 Bertelli G., Bressan A., Chiosi C., Fagotto F., Nasi E., 1994, *A&AS*, 106, 275  
 Bower R. G., Benson A. J., Malbon R., Helly J. C., Frenk C. S., Baugh C. M., Cole S., Lacey C. G., 2006, *MNRAS*, 370, 645  
 Bruzual G., Charlot S., 2003, *MNRAS*, 344, 1000  
 Cappellari M., Copin Y., 2003, *MNRAS*, 342, 345  
 Cappellari M., Emsellem E., 2004, *PASP*, 116, 138  
 Couch W. J., Sharples R. M., 1987, *MNRAS*, 229, 423  
 Courteau S., 1997, *AJ*, 114, 2402  
 Dressler A., Gunn J. E., 1982, *ApJ*, 263, 533  
 Dressler A., Gunn J. E., 1983, *ApJ*, 270, 7  
 Emsellem E. et al., 2007, *MNRAS*, 379, 401  
 Faber S. M., Jackson R. E., 1976, *ApJ*, 204, 668  
 Faber S. M. et al., 1997, *AJ*, 114, 1771  
 Georgakakis A. et al., 2008, *MNRAS*, 385, 2049  
 Goto T. et al., 2003, *PASJ*, 55, 771  
 Goto T., Kawai A., Shimono A., Sugai H., Yagi M., Hattori T., 2008, *MNRAS*, 386, 1355  
 Helou G., Soifer B. T., Rowan-Robinson M., 1985, *ApJ*, 298, L7  
 Jacoby G. H., Hunter D. A., Christian C. A., 1984, *ApJS*, 56, 257  
 Kennicutt R. C., 1998, *ARA&A*, 36, 189  
 Kormendy J., Djorgovski S., 1989, *ARA&A*, 27, 235  
 McGee S. L., Balogh M. L., Wilman D. J., Bower R. G., Mulchaey J. S., Parker L. C., Oemler A., 2011, *MNRAS*, 413, 996  
 Maraston C., 1998, *MNRAS*, 300, 872  
 Mihos J. C., Hernquist L., 1996, *ApJ*, 464, 641  
 Miller C. J. et al., 2005, *AJ*, 130, 968  
 Naab T., Burkert A., 2003, *ApJ*, 597, 893  
 Naab T., Burkert A., Hernquist L., 1999, *ApJ*, 523, L133  
 Norton S. A., Gebhardt K., Zabludoff A. I., Zaritsky D., 2001, *ApJ*, 557, 150  
 Poggianti B. M., Smail I., Dressler A., Couch W. J., Barger A. J., Butcher H., Ellis R. S., Oemler A. J., 1999, *ApJ*, 518, 576  
 Pracy M. B., Couch W. J., Blake C., Bekki K., Harrison C., Colless M., Kuntschner H., de Propris R., 2005, *MNRAS*, 359, 1421  
 Pracy M. B., Kuntschner H., Couch W. J., Blake C., Bekki K., Briggs F., 2009, *MNRAS*, 396, 1349  
 Pracy M. B., Couch W. J., Kuntschner H., 2010, *Publ. Astron. Soc. Australia*, 27, 360  
 Rose J. A., 1985, *AJ*, 90, 1927  
 Salim S. et al., 2007, *ApJS*, 173, 267  
 Salpeter E. E., 1955, *ApJ*, 121, 161  
 Shioya Y., Bekki K., Couch W. J., 2004, *ApJ*, 601, 654  
 Swinbank A. M., Balogh M. L., Bower R. G., Hau G. K. T., Allington-Smith J. R., Nichol R. C., Miller C. J., 2005, *ApJ*, 622, 260  
 Tran K.-V. H., Franx M., Illingworth G., Kelson D. D., van Dokkum P., 2003, *ApJ*, 599, 865  
 Tran K.-V. H., Franx M., Illingworth G. D., van Dokkum P., Kelson D. D., Magee D., 2004, *ApJ*, 609, 683  
 Tremonti C. A., Moustakas J., Diamond-Stanic A. M., 2007, *ApJ*, 663, L77  
 Vazdekis A., Arimoto N., 1999, *ApJ*, 525, 144  
 Wolf C., Gray M. E., Meisenheimer K., 2005, *A&A*, 443, 435  
 Yamauchi C., Goto T., 2005, *MNRAS*, 359, 1557  
 Yan R., Newman J. A., Faber S. M., Konidakis N., Koo D., Davis M., 2006, *ApJ*, 648, 281  
 Yan R. et al., 2009, *MNRAS*, 398, 735  
 Yang Y., Zabludoff A. I., Zaritsky D., Lauer T. R., Mihos J. C., 2004, *ApJ*, 607, 258  
 Yang Y., Zabludoff A. I., Zaritsky D., Mihos J. C., 2008, *ApJ*, 688, 945  
 Zabludoff A. I., Zaritsky D., Lin H., Tucker D., Hashimoto Y., Sheckman S. A., Oemler A., Kirshner R. P., 1996, *ApJ*, 466, 104

This paper has been typeset from a  $\text{\TeX}/\text{\LaTeX}$  file prepared by the author.